Modeling, Identification and Control, Vol. 46, No. 3, 2025, pp. 101–109, ISSN 1890–1328

Hydraulic accumulator fault diagnosis using LSTM neural networks

P. Olszewski [1] K. F. Pajuro [1] L. B. Hansen [1] L. S. Ramos [1] M. K. Odena [1] J. Liniger [1]

[1] *AAU Energy, Aalborg University, DK6700 Esbjerg, Denmark. E-mail:* jel@energy.aau.dk

Abstract

The maintenance costs associated with offshore wind turbines, particularly those related to logistics and system downtimes, are significantly influenced by the reliability of hydraulic components, especially the pitch control system. Accumulator failures, which constitute a notable percentage of system faults, often result from gas leakage and pressure drops, highlighting the need for efficient fault detection and diagnosis (FDD) methods. This paper presents a novel approach utilizing Long Short-Term Memory (LSTM) neural networks for detecting faults in hydraulic accumulators. Two LSTM models were developed: a regression model that estimates the exact pre-charge pressure and a classification model that predicts pressure ranges. The models were trained and validated using both experimental and simulation data from a hydraulic test setup. Results demonstrated that the regression network achieved a root mean square error (RMSE) of approximately 4.2 bar, while the classification network reached 78.75% accuracy. The findings show that LSTM networks provide precision similar to prior art but for a larger variation of load cases. Thus, the proposed non-invasive method is promising for early fault detection in offshore wind turbine accumulators, potentially reducing operational costs and enhancing maintenance strategies.

Keywords: fluid power, hydraulic accumulator, fault detection and diagnosis, gas leakage, LSTM, offshore wind

1 Introduction

The operational expenditures (OpEx) for offshore wind turbines are significantly impacted by the costs associated with travel and maintenance activities, which are both costly and time-consuming. Among the various components of wind turbines, the pitch control system has been identified as a critical area where most faults occur, contributing notably to the overall downtime and maintenance costs. Specifically, 10.5% of these failures are attributed to issues within the accumulator, a key component responsible for maintaining hydraulic pressure in the pitch control system (Carroll et al. (2016); Liniger et al. (2017c)). Partly, accumulator failures are caused by gas leakage resulting in a decrease in pre-charge pressure.

Elorza et al. (2022) developed a sensor data processing algorithm for diagnosing hydraulic pitch system faults. Specifically for accumulator gas leakage, the algorithm was able to detect a 50% drop in pre-charge pressure. It was noted that the pitch system function was not inhibited due to this seemingly large magnitude of gas leakage. This algorithm, distinct from other model-based approaches, requires minimal local sensor data processing, validated through synthetic data generated by simulation software. As noted by Elorza et al., the method needs experimental investigation to evaluate the efficiency in realistic conditions. Furthermore, advanced methods employing multivariate statistics (Helwig et al. (2015)), multi-resolution signal decomposition (Liniger et al. (2017b)), and Extended Kalman Filters (EKF) (Liniger et al. (2017a)) have been explored for fault detection. Recent ap-

doi:10.4173/mic.2025.3.1

proaches also include the use of a bank of EKFs and State Augmented EKFs incorporating surface temperature measurements for enhanced fault detection capabilities (Asmussen et al. (2022)). The latter indicates the remaining amount of gas, yet with an offset of ±10% corresponding to a 4.2 bar RMSE. In general, the methods specifically developed for accumulator gas leakage detection provide an opportunity for fault detection; a higher fidelity is needed to assess how the fault develops and ultimately gives an early warning of the need for maintenance.

Recent investigations have shown promising results from using neural network architectures for condition monitoring and fault detection, particularly in wind turbines and gearboxes. Xiang et al. (2021) proposed a model combining convolutional neural networks (CNN) and long short-term memory (LSTM) with an attention mechanism to process SCADA data for wind turbine fault detection. The CNN extracts dynamic features, while the LSTM models time dependencies. Attention mechanisms further enhance critical feature extraction, improving fault prediction accuracy and enabling early anomaly detection. Chen et al. (2022) introduced a physics-informed hyperparameter selection strategy for LSTM to enhance gearbox fault detection. By integrating domain-specific physical knowledge into the model's training process, the proposed method achieves better differentiation between healthy and faulty states compared to traditional LSTM setups. Lei et al. (2019) utilize LSTM networks for wind turbine fault diagnosis by leveraging their capability to model long-term dependencies in time-series data. Their results suggest that LSTM outperforms conventional methods like support vector machines (SVM) and CNN in handling multivariate time-series data, achieving robust fault classification even with limited data. Chen et al. (2021) developed a hybrid model integrating LSTM with an autoencoder (AE) for anomaly detection in wind turbines. The model identifies critical parameters contributing to performance anomalies, offering both fault detection and root cause analysis. Zhu et al. (2022) proposed a combination of LSTM, fuzzy synthesis, and transfer learning for wind turbine gearbox monitoring. This approach leverages limited faulty data samples by transferring learned knowledge between similar turbines, enhancing fault detection accuracy while reducing dependence on extensive labeled datasets. He et al. (2023) introduced a ResLSTM model integrating residual learning and attention mechanisms for time-series forecasting in wind turbine condition monitoring. This method effectively addresses issues like gradient vanishing in deep networks and captures critical temporal features from SCADA data.

Given the challenges of accumulator gas leakage detection and opportunities of LSTM-based fault detection, this paper aims to explore the potential of both regression and classification LSTM-based methods for detecting gas leakage in hydraulic accumulators. The approach offers a promising alternative for increasing fault detection accuracy while maintaining the simplicity of the physical system configuration. The training uses an augmented set of experimental and simulated data. The sensor configuration in our study follows a similar setup as presented by Asmussen et al. (2022), where the oil pressure and accumulator oil, surface, and, ambient temperatures are used. The accumulator surface temperatures provides an indicative of the piston position as the gas undergoes a compression cycle and has shown to improve gas leakage detection performance.

2 Accumulator system description

A physical hydraulic setup at Esbjerg campus of Aalborg University was used in generation of experimental data for both tuning of a simulation model and a training set.

2.1 Experimental setup

The setup can be seen in Figure 1 and is designed for the investigation of accumulator operation similar to the conditions in wind turbines. A hydraulic piston accumulator consists of a gas chamber and an oil chamber separated by a piston as shown in Figure 3. The gas chamber of the accumulator is charged with nitrogen. The pre-charge pressure is the amount of gas charged in the accumulator with no oil, given for a gas temperature of 20°. When the oil pressure exceeds the precharge pressure, the piston starts moving, compressing the gas.

The accumulator used in the setup is HYDAC SK350-25, which has a volume of 25l. The accumulator is discharged during experiments through a proportional valve (4WREE). This valve is actuated by a controller to match flow measured through it (Q_l) to a given load flow. Valve V1 is used through on/off control to keep pressure at the accumulator within 175 bar and 200 bar. Valve V2 is used to discharge the accumulator at the end of an experiment.

The experimental data is collected from accumulator pressure sensor p_a and oil temperature sensor T_p. Additionally, ten temperature sensors were installed on the surface of the accumulator, which can be seen in Figure 2. All sensors are spread uniformly across the length of the accumulator, with one sensor being in

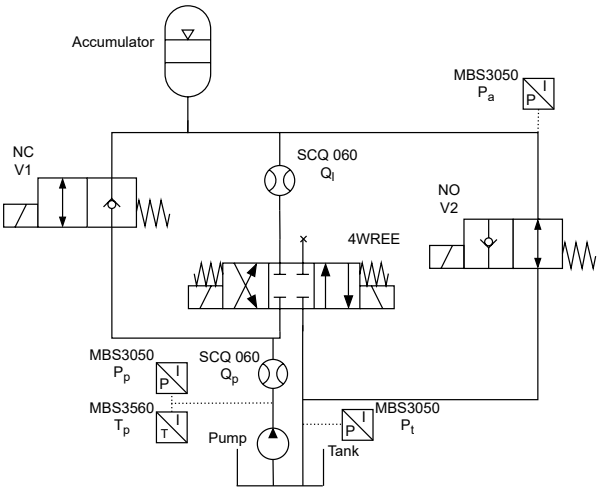

Figure 1: Diagram of the physical hydraulic system.

the area of the end cap. One last temperature sensor is measuring ambient temperature.

The data from the setup was collected at pre-charge pressures 110, 120, 130, 140, 150 bar. As input, three load flows of a wind turbine hydraulic pitch system were used based on configuration one by Liniger et al. (2017a).

2.2 Simulation model

In addition to experimental data, this study utilizes data from a simulation model of the accumulator. The hydraulic accumulator model is divided into three parts: a mechanical model, the gas equation of state, and the thermal model.

The mechanical model describes the movement of the piston in the accumulator, given by Newton's second law of motion:

$$\ddot{x}_p m_p = (p_a - p_g)\, A_{op} - F_{fric} \tag{1}$$

where m_p is the mass of the piston, p_a is the accumulator oil pressure, p_g is the gas pressure, A_{op} is the piston area, and F_{fric} is the friction force described as:

$$F_{fric} = B\dot{x}_p + C \tag{2}$$

where B is the viscous friction constant and C is the Coulomb friction constant.

The gas equation of state describes the relation between the states of the gas such as temperature, pressure, and volume. The Benedict-Webb-Rubin (BWR) empirical equation of state is used for the accumulator model following the work by Goldfrank and Cooper (1967).

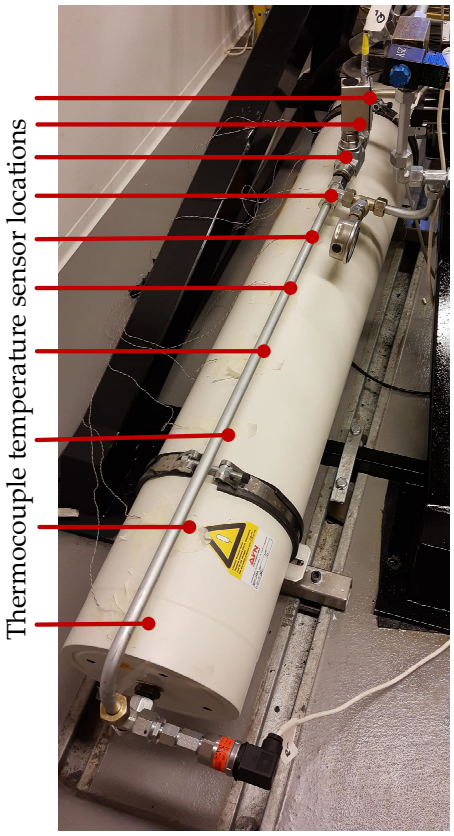

Figure 2: Placement of temperature sensors on the top surface of the hydraulic accumulator.

The BWR equation of state is shown below:

$$p_g = \frac{RT_g}{v} + \frac{B_0 RT_g - A_0 - \frac{C_0}{T_g^2}}{v^2} + \frac{bRT_g - a}{v^3} + \ldots \\ \frac{a\alpha}{v^6} + \frac{c\left(1+\frac{\gamma}{v^2}\right)e^{-\frac{\gamma}{v^2}}}{v^3 T_g^2} \tag{3}$$

where v is the specific volume, T_g is the gas temperature, and $A_0, B_0, C_0, a, b, c, \alpha, \gamma, R$ are constants for nitrogen.

The thermal model of the accumulator is divided into three parts: the accumulator piston, the end-cap of the accumulator towards the gas inlet, and the accumulator wall. The wall is further divided into eight elements. The model is inspired by model two as described by Pfeffer et al. (2016). The temperature of the end-cap of the accumulator towards the oil inlet is assumed to be equal to the oil temperature. The end-cap of the accumulator is modeled as a single body with a uniform temperature and the temperature change of the end-cap is described by the energy balance given as:

$$\dot{T}_e = \frac{\dot{Q}_{ge} + \dot{Q}_{ae}}{m_e c_{steel}} \tag{4}$$

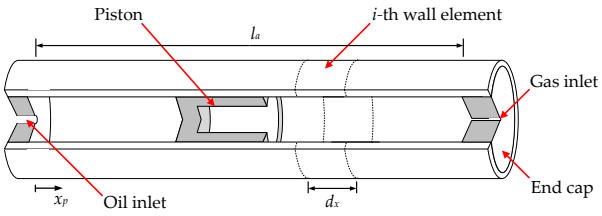

Figure 3: Piston accumulator with model notation.

where T_e is the temperature of the end cap, m_e is the mass of the end-cap, c_{steel} is the specific heat capacity of steel, and $\dot{Q}_{ge}$ and $\dot{Q}_{ae}$ are the heat flows from the gas and air to the end-cap respectively. $\dot{Q}_{ge}$ is given as:

$$\dot{Q}_{ge} = \alpha_g A_{eg} \left(T_g - T_e\right) \tag{5}$$

and $\dot{Q}_{ae}$ is described as:

$$\dot{Q}_{ae} = \alpha_a A_{ea} \left(T_a - T_e\right) \tag{6}$$

where α_a is a convective heat transfer coefficient between air and steel, α_g is a convective heat transfer coefficient between gas and steel, A_{ea} is the surface area between the end-cap and air, A_{eg} is the surface area between the end-cap and gas, and T_a is the temperature of the ambient air.

The piston is modeled similarly to the end cap as a single body with a uniform temperature. The heat flux between the piston and accumulator wall is neglected since the piston is suspended by sealing rings. The heat transfer coefficients of the sealing ring materials are typically much lower than those present for oil or gas to steel. The energy balance of the piston is:

$$\dot{T}_p = \frac{\dot{Q}_{gp} + \dot{Q}_{op}}{m_p c_{steel}} \tag{7}$$

where T_p is the temperature of the piston, m_p is the mass of the piston, and $\dot{Q}_{gp}$ and $\dot{Q}_{op}$ are the heat flows from the gas and oil to the piston, respectively. $\dot{Q}_{gp}$ is given as:

$$\dot{Q}_{gp} = \alpha_g A_{gp} \left(T_g - T_p\right) \tag{8}$$

and $\dot{Q}_{op}$ is given as:

$$\dot{Q}_{op} = \alpha_o A_{op} \left(T_o - T_p\right) \tag{9}$$

where α_o is a convective heat transfer coefficient between oil and steel and A_{gp} and A_{op} are the surface areas of the piston towards the gas and the oil, respectively.

The accumulator wall is divided into $n = 8$ elements where the temperature is considered uniform for each wall element. The energy balance for each element can be divided into a convective part and a conductive part as shown below:

$$\dot{T}_w^{[i]} = \dot{T}_{convective}^{[i]} + \dot{T}_{conductive}^{[i]} \tag{10}$$

where $T_w^{[i]}$ is the i'th wall element temperature and $i = 1, 2, \cdots, n$. The convective heat flow for the i'th element can be described as:

$$\dot{T}_{convective}^{[i]} = \frac{\dot{Q}_{aw}^{[i]} + \dot{Q}_{ow}^{[i]} + \dot{Q}_{gw}^{[i]}}{\rho\, c_{steel} \left(r_{os}^2 - r_{is}^2\right) \pi d_x} \tag{11}$$

where r_{os} and r_{is} are the outer and inner radii of the accumulator and d_x is the length of the wall element. The convective heat flows, $\dot{Q}_{aw}$, $\dot{Q}_{ow}$, and $\dot{Q}_{gw}$ are calculated as:

$$\dot{Q}_{ow}^{[i]} = \alpha_o A_{ow} \left(T_o - T_w^{[i]}\right) \xi_o^{[i]} \tag{12}$$

$$\dot{Q}_{gw}^{[i]} = \alpha_g A_{gw} \left(T_g - T_w^{[i]}\right) \xi_g^{[i]} \tag{13}$$

$$\dot{Q}_{aw}^{[i]} = \alpha_a A_{aw} \left(T_a - T_w^{[i]}\right) \tag{14}$$

where the areas are defined in such a way that A_{aw} is the area of a wall element in contact with air, A_{ow} is the area of a wall element in contact with oil, and , A_{gw} is the wall area in contact with oil. ξ_o and ξ_g describe the ratio of the wall elements in contact with oil or gas. ξ_o is given as:

$$\xi_o^{[i]} = \begin{cases} 1 & \text{for} \quad x_p > i\, d_x \\ \dfrac{x_p - (i-1)d_x}{d_x} & \text{for} \quad i\, d_x \le x_p \le i\, d_x \\ 0 & \text{for} \quad x_p < i\, d_x \end{cases} \tag{15}$$

and ξ_g is given as:

$$\xi_g^{[i]} = \begin{cases} 0 & \text{for} \quad x_p + l_p > i\, d_x \\ 1 - \dfrac{x_p - l_p + i\, d_x}{d_x} & \text{for} \quad (i-1)d_x \le x_p + l_p \le i\, d_x \\ 1 & \text{for} \quad x_p + l_p < i\, d_x \end{cases} \tag{16}$$

The conductive part of the energy balance for a wall element, shown in Equation (17), is described by Fourier's law of heat conduction:

$$\dot{Q} = -\lambda \nabla T \tag{17}$$

where λ is the conductivity and ∇T is the temperature gradient. Due to the symmetry of the cylinder, the conductive heat transfer is assumed to be one-dimensional and can thus be described as:

$$\dot{Q}_{conductive} = \frac{\partial}{\partial x} \lambda \frac{\partial T_w}{\partial x} \tag{18}$$

where x is the axial direction of the accumulator.

When estimating the conductive heat flow, $\dot{Q}_{conductive}$, by a second-order central difference

equation, the conductive part of the energy balance for each wall element can be found as:

$$\dot{T}^{[i]}_{conductive} = \frac{\lambda}{\rho\, c_{steel}} \frac{T_w^{[i+1]} - 2T_w^{[i]} + T_w^{[i-1]}}{{d_x}^2} \tag{19}$$

where d_x is the length of the wall element as shown in Figure 3. The end conditions are set to the temperature of the accumulator end-cap and the oil temperature.

The total heat flow from the gas to the accumulator is defined as:

$$\dot{Q}_s = \left(\sum_{i=1}^{n} \dot{Q}^{[i]}_{gw} \right) + \dot{Q}_{gp} + \dot{Q}_{ge} \tag{20}$$

The model's response is validated against the physical system through an experiment. The model constants used for verification are given in Table 1.

Table 1: Accumulator model constants.

Symbol	Constant	Value	Unit
r_i	Internal radius	0.09	m
r_o	External radius	0.11	m
l_i	Internal length	0.983	m
l_p	Length of the piston	0.11	m
d_x	Length of one wall element	0.123	m
A_{aw}	External area of conductive heat flow of wall element	0.0849	m^2
A_{ow}, A_g	Internal area of conductive heat flow of wall element	0.0695	m^2
A_p	Piston cross-section area	0.0254	m^2
A_{ae}	Area for heat flux between air and end cap	0.038	m^2
A_{ge}	Area for heat flux between gas and end cap	0.0254	m^2
V_p	Precharge volume	0.0222	m^3
m_p	Mass of the piston	7.86	kg
m_e	Mass of the end cap	19.95	kg
ρ	Density of steel	7810	$\frac{kg}{m^3}$
c_{N_2}	Specific heat capacity of nitrogen	741.07	$\frac{k}{kg \cdot K}$
c_{steel}	Specific heat capacity of steel	502.42	$\frac{J}{kg \cdot K}$
λ	Thermal conductivity of steel	58	$\frac{W}{m \cdot K}$
α_a	Convective heat transfer coefficient of the air	20	$\frac{W}{m^2 \cdot K}$
α_o	Convective heat transfer coefficient of the oil	100	$\frac{W}{m^2 \cdot K}$
α_g	Convective heat transfer coefficient of the gas	25	$\frac{W}{m^2 \cdot K}$

The accumulator is first fully discharged then recharged while recording sensor data. The input flow for the model is derived from the measured piston position. The piston position, x_p, and accumulator oil pressure, p_a, is compared in Figure 4, showing close agreement. The mean error is 0.36 mm for piston position and 2.04 bar for pressure.

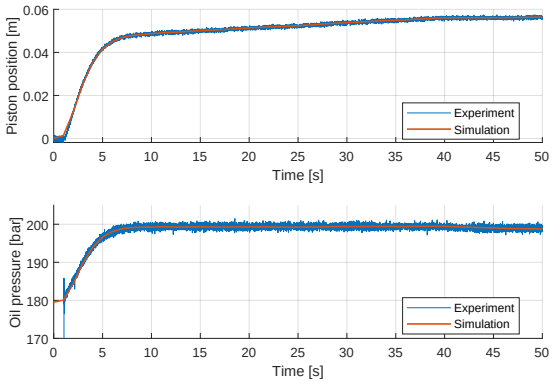

Figure 4: Simulation and experiment comparison of piston position and accumulator oil pressure.

Temperature validation is given in Figure 5. The timespan is extended to 1500 seconds, focusing on wall element $i = 6$. This element is chosen because the setup is equipped with temperature sensors on both the top and bottom of the accumulator element to assess the uniform temperature assumptions. Simulated temperatures matched the experimental data trends, staying within the range of expected top and bottom temperatures. The model is tuned to match the top temperature, since these sensors are used further for both the training and validation data.

3 Proposed method

This paper presents a method employing LSTM neural networks to estimate the accumulator pre-charge pressure. Two types of LSTM networks are developed and evaluated: a regression network and a classification network. The regression network provides real-time estimations of the current pre-charge pressure, while the classification network determines the pressure range in

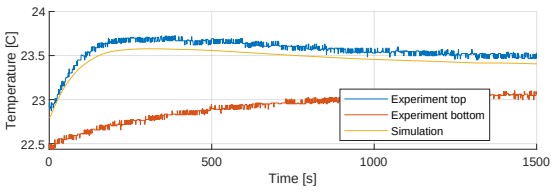

Figure 5: Simulation and experiment comparison of element $i = 6$ wall temperatures.

which the current pre-charge pressure falls. This classification offers a broader assessment, indicating whether the pressure is below the fault threshold.

By training the networks on data collected during normal accumulator operation, the method enables pre-charge pressure estimation without interrupting regular operation or requiring specific actuation.

The training data is derived from a combination of physical experiments and simulations. Simulated data is used to supplement the dataset due to the extended time required for data collection in a physical system.

3.1 LSTM networks

Two types of LSTM networks were developed for estimation of the pre-charge pressure: a regression network and a classification network. Layers of each network can be seen in Figure 6.

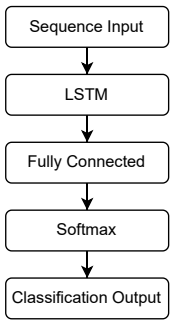

(a) Classification

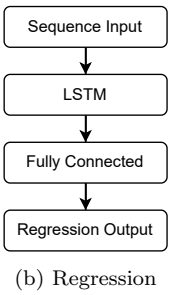

(b) Regression

Figure 6: Layers of the developed LSTM networks.

Both networks take as input a sequence of vectors of 12 measurements sampled at 1 Hz. The measurements consist of 8 wall element temperatures, endcap temperature, oil pressure, oil temperature, ambient temperature. The input is fed into an LSTM layer. This layer is configured with tanh state activation function, sigmoid gate activation function, and number of hidden units chosen in a hyper-parameter sweep.

The output of the LSTM layer is fed through one fully connected layer. For the regression network, the fully connected layer provides one output, which is the output of the predicted precharge pressure. The loss function used in this case is mean-squared-error. During network training it was found out that output normalization is required for the regression network, otherwise the training would consistently fail with the network outputting a constant value. Therefore, min-max normalization was applied, mapping values in range 95 to 165 bar, to a range from 0 to 1.

For the classification network, the fully connected layer has 7 outputs which feed through a softmax function to provide the final output. The loss function used is cross-entropy. Each output corresponds to a 10 bar wide bin in the range from 95 to 165 bar with centers at 100, 110, 120, 130, 140, 150, 160 bar.

3.2 Network training

Both the regression and the classification LSTM networks were trained using a mix of 45 cases of experimental data and 700 cases of simulation data. The experimental data was split into training, validation, testing sets in a 5:2:2 ratio. The simulated data was split in 8:1:1 ratio. The different ratio for the experimental data is due to its smaller amount as to still provide sufficient amount of cases for validation and testing sets. Each case consisted of 200 samples.

The training parameters were the following: adam solver with initial learn rate of 0.1 and mini-batch size of 150. For both networks a hyper-parameters sweep was performed to find the optimal amount of hidden units and training epochs. Results can be seen in Table 2 and 3.

Table 2: Regression LSTM hyper-parameter sweep.

Trial	Hidden Units	Epochs	Validation RMSE	Training RMSE
1	10	500	0.1417	0.0953
2	30	500	0.0993	0.0703
3	50	500	0.1855	0.0893
4	100	500	0.1849	0.1435
5	10	1000	0.1359	0.1292
6	30	1000	0.0883	0.0793
7	50	1000	0.1378	0.0801
8	100	1000	0.1679	0.0847
9	10	2000	0.1051	0.0692
10	30	2000	0.0600	0.0736
11	50	2000	0.1591	0.0659
12	100	2000	0.1616	0.1005

The final regression and classification networks, are chosen based on the results for the validation set. The best performing regression network is one from trial number 10 with 30 hidden units, trained for 2000 epochs, with normalized validation RMSE of 0.06. Its training performance can be seen in Figure 7 and results against a test set in Figure 8.

The best performing classification network is one from trial number 12 with 100 hidden units, trained for 200 epochs, with validation accuracy of 78.75%. Its training performance can be seen in Figure 9 and results against a test set in Figure 10.

Table 3: Classification LSTM hyper-parameter sweep.

Trial	Hidden Units	Epochs	Validation Accuracy	Training Accuracy
1	10	500	30.00	29.33
2	30	500	58.75	58.00
3	50	500	48.75	55.33
4	100	500	70.00	38.00
5	10	1000	41.25	51.33
6	30	1000	57.50	65.33
7	50	1000	51.25	76.00
8	100	1000	45.00	64.00
9	10	2000	40.00	49.33
10	30	2000	65.00	59.33
11	50	2000	65.00	80.67
12	100	2000	78.75	86.00

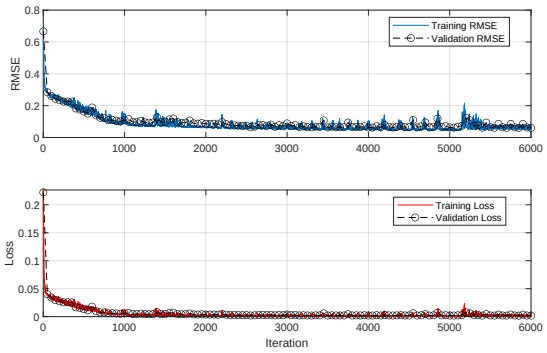

Figure 7: Regression network training RMSE and loss over training iterations.

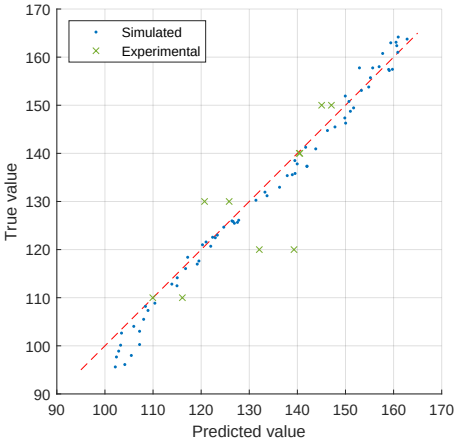

Figure 8: Regression network comparison between true and predicted values for the test set with separation between simulated and experimental data.

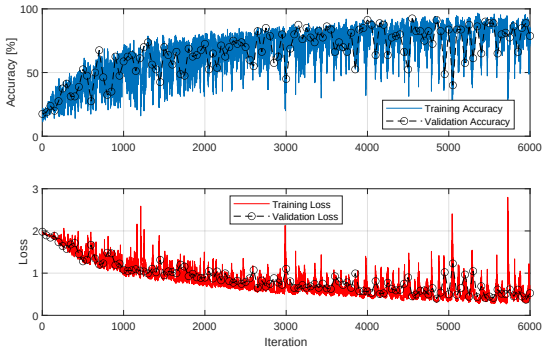

Figure 9: Classification network training accuracy and loss over training iterations.

3.3 Results and discussion

From the two trained LSTM networks, the regression network performed best with number of hidden units between 10 and 30, and with improving performance with higher amount of epochs. Overfitting was noticeable with higher number of hidden units. The best network (trial 10) estimates the pre-charge pressure with RMSE of 4.2 bar which is on par with prior art but for a larger variety of load conditions underlining the efficacy of the proposed method. The pressure is estimated well in the range of 110 bar to 165 bar. The estimation is skewed towards higher values for pressures below 110 bar, and is off by up to 7 bars. When looking at the experimental data, the network estimated pre-charge pressures at 120 bar to be higher and up to 20 bar away from the true value. This problem is not seen for other values of pre-charge pressure.

The classification network performed best with higher number of epochs and hidden units. Increased accuracy with higher amount of hidden units can be explained by the discontinuous nature of classification output. The best network (trial 12) estimates the pre-charge pressure category with 78.75% accuracy. It predicts most accurately the lowest and highest pressure. The estimations in-between are at most one category off when looking at simulated data, with majority being categorized correctly. When looking at the experimental data, all estimates for 130 bar category are 20 bar lower than the true value. For 140 bar category, all estimates are 10 bar higher. For category of 120 bar, only one estimate is higher by 20 bar.

4 Conclusion

This study developed and evaluated two types of LSTM neural networks—regression and classification models—for fault detection and diagnosis of hydraulic

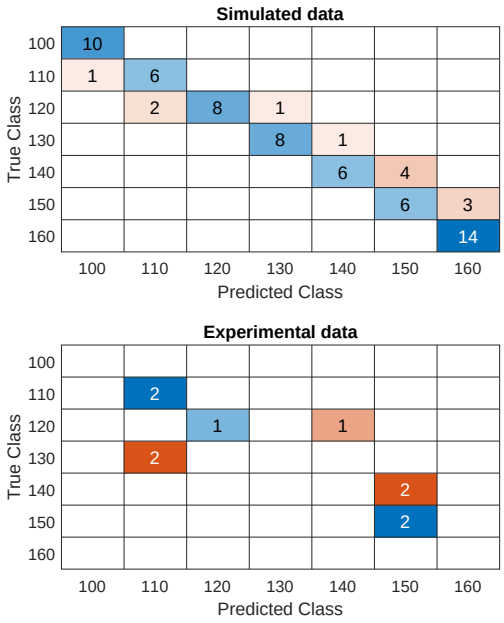

Figure 10: Classification network comparison between true and predicted values for the test set with separation between simulated and experimental data.

accumulators in offshore wind turbine pitch systems. By leveraging a combination of experimental and simulation data, both networks demonstrated the ability to estimate pre-charge pressure based on non-invasive temperature and pressure measurements, providing a cost-effective and efficient alternative to traditional fault detection methods.

The regression network achieved an RMSE of approximately 4.2 bar, showing reliable performance across most pressure ranges but encountering some inaccuracies at lower pressures. The classification network reached an accuracy of 78.75%, effectively identifying the correct pressure category, especially at the extremes. However, some discrepancies were observed, particularly when applied to experimental data. The best-performing model-based method outperforms both the classification (15%) and regression network (17%), which showed a 10% estimation error.

Future work should focus on optimizing the classification model, as it offers higher precision, making it more suitable for early fault detection and trend analysis. Additionally, exploring transfer learning could significantly reduce the need for extensive training data specific to each accumulator, enhancing the practicality of these neural network models for broader applications in wind turbine maintenance.

References

Asmussen, M. F., Liniger, J., Sepehri, N., and Pedersen, H. C. Pre-charge pressure estimation of a hydraulic accumulator using surface temperature measurements. *Wind*, 2022. 2(4):784–800. doi:10.3390/wind2040041.

Carroll, J., McDonald, A., and McMillan, D. Failure rate, repair time and unscheduled O&M cost analysis of offshore wind turbines. *Wind Energy*, 2016. 19(6):1107–1119. doi:10.1002/we.1887.

Chen, H., Liu, H., Chu, X., Liu, Q., and Xue, D. Anomaly detection and critical scada parameters identification for wind turbines based on lstm-ae neural network. *Renewable Energy*, 2021. 172:829–840. doi:10.1016/j.renene.2021.03.078.

Chen, Y., Rao, M., Feng, K., and Zuo, M. J. Physics-informed lstm hyperparameters selection for gearbox fault detection. *Mechanical Systems and Signal Processing*, 2022. 171:108907. doi:10.1016/j.ymssp.2022.108907.

Elorza, I., Arrizabalaga, I., Zubizarreta, A., Martín-Aguilar, H., Pujana-Arrese, A., and Calleja, C. A Sensor Data Processing Algorithm for Wind Turbine Hydraulic Pitch System Diagnosis. *Energies*, 2022. 15(1):33. doi:10.3390/en15010033.

Goldfrank, J. C. and Cooper, H. W. Benedict-Webb-Rubin constants and new correlations. *Hydrocarbon Processing*, 1967. 46(12).

He, Y., Liu, J., Wu, S., and Wang, X. Condition monitoring and fault detection of wind turbine driveline with the implementation of deep residual long short-term memory network. *IEEE Sensors Journal*, 2023. 23(12):13360–13371. doi:10.1109/JSEN.2023.3273279.

Helwig, N., Pignanelli, E., and Schütze, A. Condition monitoring of a complex hydraulic system using multivariate statistics. In *2015 IEEE International Instrumentation and Measurement Technology Conference (I2MTC) Proceedings*. pages 210–215, 2015. doi:10.1109/I2MTC.2015.7151267. ISSN: 1091-5281.

Lei, J., Liu, C., and Jiang, D. Fault diagnosis of wind turbine based on long short-term memory networks. *Renewable Energy*, 2019. 133:422–432. doi:10.1016/j.renene.2018.10.031.

Liniger, J., Pedersen, H. C., and Soltani, M. Model-Based Estimation of Gas Leakage for Fluid Power Accumulators in Wind Turbines. American Society of Mechanical Engineers Digital Collection, 2017a. doi:10.1115/FPMC2017-4253.

Liniger, J., Sepehri, N., Soltani, M., and Pedersen, H. Signal-Based Gas Leakage Detection for Fluid Power Accumulators in Wind Turbines. *Energies*, 2017b. 10(3):331. doi:10.3390/en10030331.

Liniger, J., Soltani, M., Pedersen, H. C., Carroll, J., and Sepehri, N. Reliability based design of fluid power pitch systems for wind turbines. *Wind Energy*, 2017c. 20(6):1097–1110. doi:10.1002/we.2082.

Pfeffer, A., Glück, T., Kemmetmüller, W., and Kugi, A. Mathematical modelling of a hydraulic accumulator for hydraulic hybrid drives. *Mathematical and Computer Modelling of Dynamical Systems*, 2016. 22(5):397–411. doi:10.1080/13873954.2016.1174716.

Xiang, L., Wang, P., Yang, X., Hu, A., and Su, H. Fault detection of wind turbine based on scada data analysis using cnn and lstm with attention mechanism. *Measurement*, 2021. 175:109094. doi:10.1016/j.measurement.2021.109094.

Zhu, Y., Zhu, C., Tan, J., Tan, Y., and Rao, L. Anomaly detection and condition monitoring of wind turbine gearbox based on lstm-fs and transfer learning. *Renewable Energy*, 2022. 189:90–103. doi:10.1016/j.renene.2022.02.061.